



Experimental evidence of the metastability of ferric smectite

Fabien Baron, Sabine Petit, Alain Decarreau

► To cite this version:

Fabien Baron, Sabine Petit, Alain Decarreau. Experimental evidence of the metastability of ferric smectite. *Geochimica et Cosmochimica Acta*, 2019, 265, pp.69-84. 10.1016/j.gca.2019.08.040 . hal-02363221

HAL Id: hal-02363221

<https://cnrs.hal.science/hal-02363221>

Submitted on 3 Dec 2020

HAL is a multi-disciplinary open access archive for the deposit and dissemination of scientific research documents, whether they are published or not. The documents may come from teaching and research institutions in France or abroad, or from public or private research centers.

L'archive ouverte pluridisciplinaire **HAL**, est destinée au dépôt et à la diffusion de documents scientifiques de niveau recherche, publiés ou non, émanant des établissements d'enseignement et de recherche français ou étrangers, des laboratoires publics ou privés.

Experimental evidence of the metastability of ferric smectite

Fabien Baron^{1,2,*}, Sabine Petit¹, and Alain Decarreau¹

¹Institut de Chimie des Milieux et Matériaux de Poitiers - IC2MP, UMR CNRS 7285, Université de Poitiers, 86022 Poitiers, France

²Laboratoire de Planétologie et Géodynamique - LPG, UMR CNRS 6112, Université de Nantes, 44300 Nantes, France

*corresponding author: Fabien Baron - fabien.baron@univ-poitiers.fr

Abstract

The stability of clay minerals, and especially ferric smectites, as a function of time, is of interest for natural environments due to their high capacity to exchange electrons that control a large part of the geochemical cycle of different redox-sensitive organic or inorganic compounds (e.g., elements, nutrients, pollutants). An experimental approach based on hydrothermal synthesis was performed for synthesizing two series of iron-rich smectite (Na-nontronite) at two pH (near 12 and 13) from 1 day to several months at 150 °C. XRD, FTIR, and HRTEM data of the synthetic products confirmed the formation of Na-nontronite for the short time duration experiments. However, the dissolution of Na-nontronite and the concomitant formation of aegirine were observed with the increase of synthesis time. The pH of crystallization fluids clearly influences the rate of the reactions. At highest pH, Na-nontronite disappeared totally after two months and aegirine and hematite were the only crystalline phases observed. The chemical compositions of solutions were over time far from the thermodynamic stability field of nontronite, but very close to that of the aegirine-hematite equilibrium, suggesting that the formation of the nontronite depends on kinetics. The formation of nanoparticulate Na-nontronite at the earlier stage of the experiments appears likely due to their specific thermodynamic properties linked to the nanoscale particle size (i.e., high surface energy and high hydration properties). However, Na-nontronites dissolve when they reach a critical size, leading to the formation of the stable assemblage aegirine and hematite.

Keywords: smectite metastability, nontronite, nanoparticle, synthesis, clay minerals, thermodynamic equilibrium

1 Introduction

The thermodynamic stability of clay minerals and especially smectites has been abundantly debated for several decades and remains an ongoing question. The stability field of smectites and their response to a biogeochemical constraint appear today a crucial point due to (i) their ubiquitous presence in earth surface/near-surface systems (Wilson, 2013), (ii) their important role in mineral-solution-life-atmosphere interactions, and (iii) their large use in chemistry and geotechnical applications (e.g. engineering barrier).

Lippmann (1982, 1979, 1977) and Eberl (1978) were among the first ones to point out the potential metastability or the unstability of clay minerals, especially smectites, illites, and interstratified illite-smectites, under Earth surface and subsurface conditions. These authors concluded from thermodynamic approaches and natural observations that the chemical formation field of these clay minerals is located far from their thermodynamic equilibrium, indicating that their formation is derived by kinetics reactions. This interpretation was supported by the fine grain size of the clay minerals. Lippmann (1982) proposed that clay minerals owe their existence and their varied properties not to equilibrium thermodynamic properties, but to kinetics inhibitions inherent to Earth surface-subsurface conditions and to their heterogeneous chemistry. May et al. (1986) failed to determine equilibrium solubility for smectites during dissolution experiments because the compositions of contact solutions are controlled by the formation of other mineral phases. These authors, as Lippmann (1982), concluded that smectites are not true equilibrium phases due to their heterogeneous nature, but persist in natural environments for kinetic reasons. By contrast, the agreement between predicted equilibria and experimental solubility studies involving smectites obtained by Kittrick (1971a, 1971b, 1971c), and Kittrick and Peryea (1989, 1988) could indicate, at least, a metastable equilibrium. The integration of different solubility studies involving chlorites, smectites, and illites allowed Aja and Rosenberg (1992) to conclude that clay minerals having variable compositions are true phases capable to attain equilibrium. Essene and Peacor (1995) then called this thermodynamic status into question, leading to an intense debate between Aja and Rosenberg (1996) and Essene and Peacor (1997). However, the latter authors favored clay minerals sequences occurring through the Ostwald's step rules (e.g., smectite to illite reaction via interstratified illite-smectite), but diverged for the irreversibility or reversibility of these clay minerals sequences at low temperatures. Ostwald's step rules state that the first precipitated phase

is usually not the thermodynamically stable phase but rather a metastable phase (Ostwald, 1897). Several discussions on Ostwald's step rules were found in the literature (see Nývlt, 1995 and references therein), including formation kinetic rates between metastable and stable phases (e.g., Morse and Casey, 1988), irreversible thermodynamics involving minimization of entropy production (e.g., Van Santen, 1984), or change of the solution structure (Nývlt, 1995). The metastability of smectite thus remains an open question, notably because very few studies were conducted to determine this status using mineral synthesis experiments.

Nontronite appears a good smectite candidate to discuss this question because it presents the advantage of being easily synthesized with a controlled crystal-chemistry in a simple chemical system (see review in Petit et al., 2017 and references therein). Nontronite is the ferric iron [Fe(III)] end-member of the dioctahedral smectite group. The dominant octahedral cation is Fe(III), but some Mg or Al are also commonly present in the octahedral sheet of natural nontronite (Fig. 1). The layer charge of nontronite is mainly tetrahedral and comes from R(III) for Si tetrahedral substitutions (R(III) being Al(III) and possibly Fe(III)). Nontronite originates from a large diversity of surface-subsurface environments at the surface of the Earth (e.g., Wilson, 2013). Fe-bearing smectites are also an important redox buffer in the subsurface environments affecting the biogeochemical cycles of elements, nutrients, and pollutants (Neumann et al., 2011; Stucki et al., 1988; Stucki, 2013). Fe-rich smectites are also widespread at the surface of Mars (Poulet et al., 2005; Mustard et al., 2008; Carter et al., 2013; Carter et al., 2015; Michalski et al., 2015), but the actual crystal chemistry and the origin of these smectites are still debated and remain an open question.

Nontronite is largely used in diverse applications such as in degradation or retention of organic compounds, reduction of the mobility of heavy metals, or potentially used for geological disposal of high-level nuclear waste (see review in Petit et al., 2017 and references therein). The use of nontronite in environmental applications implies that nontronite must be stable for a long period at the human scale. The stability field and the evolution of nontronite over time are consequently important questions.

The objectives of the present study are to study the metastability of nontronite by evidencing mineralogical and crystal-chemical reactions involving nontronite as a function of time and to determine if the metastability of nontronite is only due to its large chemical heterogeneity. To address these questions, mineral synthesis experiments were conducted from 1 day to several

months at 150 °C using the simplest Na-Fe(III)-Si-O-OH chemical system. Full characterization of synthetic products was made to show the potential mineralogical reactions over time. The solution in contact with synthetic products was also analyzed to highlight the evolution of the physico-chemical parameters variations induced by mineralogical reactions. Thermodynamic calculations were also performed to determine the stability field of nontronite and to assess the reaction pathway.

2 Materials and methods

2.1 Synthesis of Fe(III)-nontronites

Fe(III)-nontronites were synthesized from a co-precipitated gel having a Fe/Si of 0.73 according to the procedure described in Baron et al. (2016). Two series of Fe(III)-nontronites were synthesized at 150 °C under equilibrium vapor pressure using Teflon[®] metallic-coated hydrothermal reactors (Parr[®], reactor number: 4744). The powdered gel precursor (0.5 g) was placed in contact with 30 mL of NaOH solutions at 0.01 M concentration for the first series (pH_i = 12) and at 0.15 M concentration for the second series (pH_i = 13.3) (Table 1). For both series, syntheses were performed for 1, 15, 31, 62, and 183 days. The 6 days samples were taken from Baron et al. (2016). A temperature of 150 °C was chosen according to Decarreau et al. (2008, 2004), to obtain Fe(III)-nontronites with the best crystallinity and prevent, theoretically, the crystallization of aegirine. Moreover, a synthesis temperature of 150 °C can be considered suitable to extrapolate with temperatures of clay minerals formation at the Earth surface (Petit et al., 2017). After the hydrothermal treatment, solid materials were collected by filtration (<0.1 µm) and crushed in agate mortar after a drying step of 24 hrs at 45 °C. The volume of experimental solutions decreased linearly as a function of synthesis time due to some small uncontrolled leaks. The lost volume followed this relation: $V_{\text{lost}} \text{ (mL)} = -0.044 \times N_{\text{day}} + 29.92$ ($R^2 = 0.99$) with V_{lost} = volume of lost water and N_{day} = number of days.

2.2 Characterization of the synthetic materials

A Jeol 2100 UHR (LaB₆) transmission electron microscope at 200 kV equipped with an Energy Dispersive X-ray Spectrometer (EDS) was used for High-Resolution Transmission Electron Microscopy (HRTEM) and Transmission electron microscopy (TEM) observations. For

observations, samples were dispersed in deionized water using sonication. A droplet of the suspension was then placed on a TEM copper grid and dried at ambient temperature.

Mid-infrared (MIR) spectra were obtained using a Magna-IR 760 Nicolet spectrometer equipped with an Ever-Glo source, a KBr beam splitter, and a DTGS-KBr detector. MIR spectra resulted from the average of 100 scans acquired in transmission mode over the 400 - 4000 cm^{-1} range with a resolution of 4 cm^{-1} . For analyses, KBr pellets were obtained by mixing 1 mg of powdered samples with 150 mg of KBr, and pressed at 8 kbar and then dried at 110 °C.

Powder X-ray diffraction (XRD) patterns were recorded using a Bruker D8 advance diffractometer equipped with a $\text{CuK}\alpha$ radiation, a tension of 40 kV and a current of 40 mA. Over the 2 - 57 °2 θ range, a step size of 0.025 °2 θ and a counting time of 0.6 s were used. For the (06.33) reflection, a step size of 0.025 °2 θ and a counting time of 0.6 s were used over the 57 - 63 °2 θ range.

2.3 Characterization of the experimental solutions

The pH of the starting solutions (pH_i) and the pH of solutions at the end of syntheses (pH_f) were measured at 25 °C with a FiveEasyTM Mettler Toledo (pH \pm 0.04) calibrated with three buffer solutions at pH 7.01, 10.14 and 12.00 (Table 1).

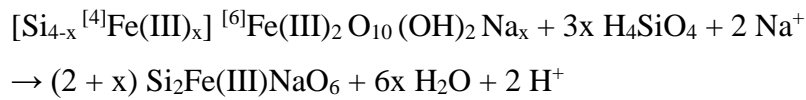
The total aqueous Si concentrations of the solutions at the end of the synthesis were measured using the molybdenum blue method from Strickland and Parsons (1972), using a Jenway 6300 spectrophotometer setting at 820 nm (Table 1). The solutions recovered by filtration (<0.1 μm) at the end of the synthesis were diluted in Milli-Q[®] pure water (18 M Ω .cm) to measure the total aqueous Si concentrations in the linear range of the calibration curve. Total aqueous sodium (Na) concentration was measured from filtrated <0.1 μm solutions using atomic absorption spectroscopy (AAS) with a Varian[®] AA240FS spectrometer (Table 1). Solutions were diluted in 2 wt. % HNO_3 to measure aqueous concentrations in the linear range of the calibration curve (i.e. from 8.26×10^{-6} to $4.35 \times 10^{-5} \text{ mol}\cdot\text{L}^{-1}$). Solutions were prepared in KNO_3 solution with a final concentration of 0.05 $\text{mol}\cdot\text{L}^{-1}$ to reduce the Na ionization in the flame during measurements.

2.4 Thermodynamic calculations

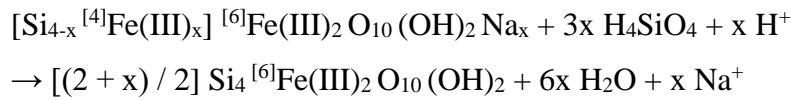
Activities of H^+ , Na^+ (aq), and H_4SiO_4 (aq) for the different syntheses were calculated at 150 °C from chemical analyses using Phreeqc[®] software (Parkhurst and Appelo, 2013) associated with the thermoddb database (thermoddb.brgm.fr) (Table 2). Thermodynamic data of aegirine and

hematite were taken from Robie and Hemingway (1995) and Hemingway (1990), respectively (included in the thermoddem database) (Table 3). Thermodynamic data of nontronites and ferripyrophyllite were obtained using the prediction model of thermodynamic properties of clay minerals developed by Blanc et al. (2015) and added in the thermoddem database (Table 3). The stability fields of nontronite ($[\text{Si}_{4-x}^{[4]}\text{Fe(III)}_x]^{[6]}\text{Fe(III)}_2\text{O}_{10}(\text{OH})_2\text{Na}_x$) with different $^{[4]}\text{Fe(III)}$ content ($x = 0.5, 0.75, 1.15$ and 1.35), aegirine ($\text{Si}_2\text{Fe(III)NaO}_6$), hematite (Fe_2O_3), and ferripyrophyllite ($\text{Si}_4^{[6]}\text{Fe(III)}_2\text{O}_{10}(\text{OH})_2$) were calculated at 150°C and assuming a constant activity of water using the six following equilibrium reactions:

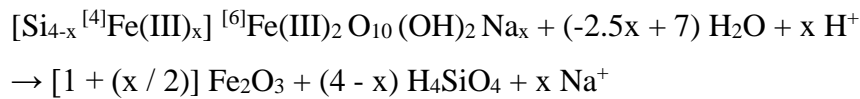
nontronite - aegirine



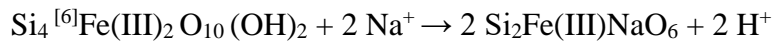
nontronite - ferripyrophyllite



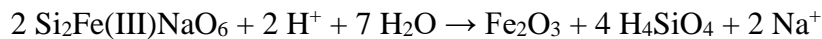
nontronite - hematite



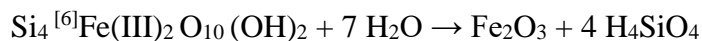
ferripyrophyllite - aegirine



aegirine - hematite



ferripyrophyllite - hematite



For the six reactions, Fe was treated as an inert compound in the sense of Thompson (1955) on the basis of the lack of dissolved Fe in solutions (see below). The $^{54}\text{Fe(III)}$ contents (x) of nontronites were fixed taking into account the structural formula of the synthesized nontronites.

3 Results

3.1 Chemical properties of solutions

The evolution of pH_i , pH_f and total aqueous concentrations of Si and Na with time are given in Table 1. For all syntheses (except sample NT35) the pH_f values are always lower than pH_i values. This trend is linked to the consumption of OH groups during the dissolution of the gel precursor and the precipitation of hydroxylated minerals (Decarreau, 1985). The total aqueous concentration of Fe was assumed to be in the same order as in Baron et al. (2016); i.e., at least two orders of magnitude lower than those of Na and Si.

3.2 Characterization of solid materials

3.2.1 Starting gel

The XRD pattern of the gel precursor exhibits: i) a broad reflection at 13.6 \AA , that could be due to the occurrence of some TOT-like layers (Decarreau et al., 2008); ii) a clear increase in the overall diffracted intensities around 30° (2θ) characterizing the high proportion of poorly organized material (Figs. 2 and 3). The MIR spectrum of the gel precursor has similarities with that of synthesized nontronite (Fig. 4). In the OH stretching (ν) region ($3700 - 3200 \text{ cm}^{-1}$), a shoulder is observed at 3555 cm^{-1} and corresponds to the 3560 cm^{-1} band attributed to $\nu \text{ Fe}^{3+}_2\text{-OH}$ vibrations as for the crystallized nontronite (see below). The broad band at 3400 cm^{-1} is attributed to large amounts of adsorbed water (Fig. 4). In the $1200\text{-}400 \text{ cm}^{-1}$ region, the broad bands observed for the gel appear at the same wavenumbers ranges as for the synthesized nontronite (Fig. 4). Thus, IR and XRD data suggest the occurrence of TOT-like structures in the gel precursor. Layered structures could not be identified from HRTEM observations which reveal aggregates composed of rounded particles (Fig. 5a), that rather exhibit an amorphous state (Fig. 5b).

3.2.2 Nontronite series synthesized at $\text{pH}_i = 12$

Powder XRD patterns of samples exhibit reflections at 12.59 \AA (001), 4.58 \AA (02-11), 3.11 \AA (004), 2.62 \AA (13-20), and $1.528 - 1.537 \text{ \AA}$ (06,33) (Fig. 2) corresponding to Na-nontronite (Brindley and

Brown, 1980; Decarreau et al., 2008). No other crystalline material has been identified in any samples. The shift of the (06,33) reflection from 1.528 Å (1, 6, 15 days samples) to 1.537 Å (62,183 days samples) reflects the increase in total Fe(III) content in the smectite structure (Eggleton, 1977; Brigatti, 1983; Köster et al., 1999; Heuser et al., 2013; Petit et al., 2015), and more precisely, for strictly Fe(III)-synthesized nontronites, the increase in the amount of Fe(III) - for - Si(IV) tetrahedral substitutions (Petit et al., 2015; Baron et al., 2016) (Fig. 2b). The apparent full width at half-maximum (FWHM) of the (00l) reflection (c^* axis) and the (06, 33) one (ab plane) decreases with synthesis time (Fig. 2b) due to, respectively, an increase in the number of regularly stacked layers and a better crystallinity in the layer plane of nontronite particles.

MIR spectra of all samples (Fig. 6), exhibit an absorption band at 3560 cm^{-1} attributed to the stretching $\nu \text{Fe}^{3+}_2\text{-OH}$ vibrations characterizing synthetic as well as natural nontronites (Goodman et al., 1976; Gates, 2005; Gates, 2008; Decarreau et al., 2008; Petit et al., 2015; Baron et al., 2016; Madejová et al., 2017). However, the intensity of this band, when normalized to the main $\nu \text{Si-O}$ band (997- 1012 cm^{-1}), increases over synthesis time whereas the FWHM decreases (Table 4). These observations substantiate the increase in crystallinity of the nontronite samples with the synthesis time (Decarreau et al., 2008; 2014). This trend is well correlated with the increase in intensity of the band at 815 cm^{-1} (Fig. 6) attributed to the bending (δ) $\text{Fe}^{3+}_2\text{-OH}$ vibrations (Goodman et al., 1976; Gates, 2005; Gates, 2008; Decarreau et al., 2008; Petit et al., 2015; Baron et al., 2016; Madejová et al., 2017). The $\nu \text{Si-O}$ band is located at 1012 cm^{-1} for the 1 day sample, and shifts down to 997 cm^{-1} for the 62 and 183 days samples (Fig. 6, Table 4). Simultaneously, the intensity of the band at 706 cm^{-1} due to $^{[4]}\text{Fe}^{3+}\text{-O}$ increases and the $\text{Si}^{4+}\text{-O-}^{[6]}\text{Fe}^{3+}$ absorption band shifts from 493 cm^{-1} up to 488 cm^{-1} (Decarreau et al., 2008; Petit et al., 2015; Baron et al., 2016). These features indicate an increase in the $^{[4]}\text{Fe(III)}$ content of the synthetic nontronites (Petit et al., 2015; Baron et al., 2016) which is estimated from the position of the $\nu \text{Si-O}$ band using the equation given by Baron et al. (2016). The $^{[4]}\text{Fe(III)}$ (x) content evolves from 0.46 (1 day sample) to 0.73 (183 days sample) per half-unit formula (Table 4). MIR spectra of samples obtained after 62 and 183 days of synthesis are very similar (Fig. 6) revealing the absence of structural evolution between these two samples.

The MIR spectrum of the 183 days sample exhibits discrete shoulders at 962 cm^{-1} , 647 cm^{-1} , and 565 cm^{-1} due to the occurrence of aegirine (Fig. 6) (Zhang et al., 2002), although aegirine is not identified in the corresponding XRD pattern (Fig. 2).

TEM observations of the 1 day, 6 days, 31 days, and 183 days samples reveal nontronite particles, forming foliated aggregates characteristic of smectites (Fig. 7). The 1 day sample exhibits a particle size heterogeneity (the diameter of particles varies from 10 - 50 nm up to > 100 nm) and contains some free lath-shaped nontronite particles of one hundred nm in length (Fig. 7a and 7b). The particle size heterogeneity decreases for the 6 days sample (Figs. 7c and 7d), whereas the nontronite particles overall appear much larger and thicker (Fig. 7d). This trend reflects a growth step of nontronite particles. Lath-shaped nontronite particles are also observed in the 6 days sample (Fig. 7d). The 31 days sample is composed of some free nontronite laths of 200 up to 500 nm in length (Fig. 7e) and large aggregates of small rounded particles of around 50 - 100 nm in diameter (Figs. 7e and 7f). The 183 days sample is made of foliated aggregates composed of lath shaped nontronite particles having a relatively homogeneous size (100 - 200 nm) (Fig. 7g). This sample is also composed of some smaller rounded particles (20 - 50 nm in diameter). However, few aegirine crystals are observed in the 183 days sample (Fig. 7h). The detection of aegirine is facilitated by a higher disaggregation of this sample. No particle of hematite is identified in all samples of the experiments at $\text{pH}_i = 12$.

3.2.3 Nontronite series synthesized at $\text{pH}_i = 13.3$

Powder XRD patterns of samples having the shortest times of hydrothermal treatment (i.e., from 1 to 15 days samples) exhibit reflections at 12.19 Å (001), 4.61 Å (02-11), 2.63 Å (13-20), and 1.545 - 1.552 Å (06,33) corresponding to Na-nontronites (Fig. 3). No other crystalline phase is evidenced in these samples. The (06, 33) reflection shifts from 1.545 Å to 1.552 Å for the 1 day and 15 days samples, respectively (Fig. 3b), indicating an increase, with time, in the $^{[4]}\text{Fe(III)}$ content of synthesized nontronites as for the series synthesized at $\text{pH}_i = 12$. The XRD pattern of the 31 days sample reveals nontronite reflections and aegirine ones at 4.42 Å (011), 2.99 Å (121), 2.90 Å (310), 2.54 Å (031), 2.47 Å (-321), and 2.20 Å (-312) (Clark et al., 1969; Nolan, 1969; Redhammer et al., 2000; Decarreau et al., 2004). The (06,33) reflection of the 31 days sample appears at the same position than for the 15 days sample indicating a similar $^{[4]}\text{Fe(III)}$ content for both nontronites. For the longest experiments (i.e., for 62 days and 183 days samples), XRD patterns display aegirine reflections cited above plus the one at 6.37 Å (110) and hematite reflections at 3.67 Å (012) and 2.69 Å (104) (Brindley and Brown, 1980).

The MIR spectra of the 1, 6 and 15 days samples (Fig. 8) exhibit the absorption bands characteristic of nontronite. The ν Si-O nontronite band shifts from 974 to 962 cm^{-1} for 1 and 15 days samples, respectively (Fig. 8, Table 4). The intensity of the $^{[4]}\text{Fe}^{3+}$ -O absorption band at 711 cm^{-1} increases in intensity with the synthesis time, while the Si^{4+} -O- $^{[6]}\text{Fe}^{3+}$ band shifts from 485 cm^{-1} (1 day sample) to 483 cm^{-1} (15 days sample). All these features indicate an increase in the $^{[4]}\text{Fe(III)}$ content of synthetic nontronites (Petit et al., 2015; Baron et al., 2016). Using the equation given in Baron et al. (2016), the $^{[4]}\text{Fe(III)}$ amounts are estimated to be 1.16 (1 day sample) and 1.38 (15 days sample) per half-unit formula (Table 4). The MIR spectrum of the 31 days sample exhibits a mixture of bands attributed to aegirine (broad massif of bands between 1100 and 1020 cm^{-1} , and bands at 647, 566, and 450 cm^{-1}), and to nontronite having a high $^{[4]}\text{Fe(III)}$ content (Table 4; Fig. 8). The MIR spectra of the 62 days and 183 days samples exhibit the characteristic features of aegirine at 1071, 1044, 1023, 963, 859, 734, 647, 566, 545, 504, and 450 cm^{-1} (Fig. 8) (Zhang et al., 2002).

TEM observations of the 15 days sample show nontronite particles forming foliated aggregates characteristic of smectites, associated with aegirine crystals (Figs. 9a, 9b, and 9c). Nontronite particles exhibit a higher blocky-like shape than those having a lath shape previously observed for the series synthesized at $\text{pH}_i = 12$. Two populations of particles are observed, the first one being hundreds of nm in diameter (Fig. 9a: B) and the second one being composed of particles up to 50 nm in diameter (Fig. 9a: A). This latter population is largely composed of rounded nontronite particles (Fig. 9b). For the 31 days sample, TEM observations reveal nontronites aggregates composed of large particles of around 500 nm in diameter or rounded particles of 50 - 100 nm in diameter (Figs. 9d, 9e, and 9f). Aegirine crystals of few μm in length with a prismatic shape are also identified in association with hematite (Figs. 9e and 9f). As mentioned before, the rounded shape of nontronites particles is evidence of their partial dissolution in favor of aegirine and hematite. Finally, aegirine and hematite are the only minerals observed for the 183 days sample (Figs. 9g and 9h).

3.3 Thermodynamics

To assess the reaction pathway from nontronite to aegirine and hematite, stability fields of nontronite with different $^{[4]}\text{Fe(III)}$ content ($x = 0.5, 0.75, 1.15$ and 1.35), aegirine, hematite, and

ferripyrophyllite were calculated at 150 °C (Fig. 10). Note that, the calculated stability field of nontronite tends to enlarge with the increase in $^{[4]}\text{Fe(III)}$ content (Fig. 10).

The chemical properties of solutions at the end of synthesis (Table 2) were plotted for the series at $\text{pH}_i = 12$ in Fig. 10a and for the series at $\text{pH}_i = 13.3$ in Fig. 10b. For all syntheses realized at $\text{pH}_i = 12$, solutions are far from the stability field of nontronite, but close to the aegirine-hematite tie-line (Fig. 10a). For the series at $\text{pH}_i = 13.3$, the 1 day solution is close to the triple point aegirine-hematite-nontronite ($x = 1.15$) (Fig. 10b); most of the other solutions fall near the theoretical aegirine-nontronite ($x = 1.35$) tie-line while the 62 days solution is shifted toward the stability field of hematite (Fig. 10b). The chemistry of the experimental system, that is not stoichiometric with respect to aegirine ($\text{Fe/Si} = 0.73$ in the gel precursor instead of 0.5 for aegirine), induces the crystallization of hematite.

4 Discussion

4.1 Na-Nontronite metastability

MIR, XRD, and TEM data, whatever the value of pH_i , evidence a massive dissolution of the gel precursor in favor of the crystallization of nontronite after only 1 day of hydrothermal treatment (Fig. 11). TEM observations do not exhibit the characteristic features of amorphous solid materials (Fig. 5) in the synthetic nontronite samples (Fig. 7 and 9). TEM images reveal large aggregates of nontronite particles, which may contain some residues of the precursor. No clear hump in the overall XRD intensity above the baseline around 30° (2θ) is observed, which suggests very low amounts of remaining amorphous material in 1 day synthetic products (Fig. 2 and 3). The MIR data also argue for a massive dissolution of the starting gel in favor of the nontronite crystallization that is clearly evidenced by the shift of the ν Si-O band (Fig. 4). This fast reaction is probably facilitated by the presence of already organized TOT-like structures (i.e., building blocks) in the gel precursor as previously mentioned by Decarreau et al. (2008).

From a series of nontronites synthesized at pH from 10 up to 14 for 6 days, Baron et al. (2016) demonstrated that the increase in $^{[4]}\text{Fe(III)}$ content of the nontronites is linked to the increase of pH_f values (Fig. 12). In the present study, the $^{[4]}\text{Fe(III)}$ contents of the synthesized nontronites increase for both series of pH, that are in agreement with the slight increase in pH_f , (Fig. 12; Table 1). However, the two reactions: low $^{[4]}\text{Fe(III)}$ -nontronite > high $^{[4]}\text{Fe(III)}$ -nontronite; and nontronite > aegirine would induce a decrease in pH. Thus, the slight increase in pH_f is likely due to the

dissolution of a small amount of residual gel, trapped in smectite aggregates, in favor of the nontronite crystallization because this reaction induces an increase in pH (Decarreau, 1985). The short amount of time required to synthesize these clay minerals allows the crystal chemistry of the synthesized nontronites to evolve over time.

For the series at $\text{pH}_i = 12$, the principal phenomenon observed between 1 and 62 days is the increase in the nontronite particle size (crystal growth) and the increase in crystallinity (crystal defects resorption). The coexistence of large laths with small rounded particles (Figs. 7e and 7f) may result from the “Ostwald’s ripening” process (Ostwald, 1897); i.e., the small particles dissolve in favor of the growth of larger ones. After 62 days of hydrothermal treatment, the reaction nontronite > aegirine is observed (Fig. 11; Table 1).

For the series at $\text{pH}_i = 13.3$, nontronite is the single mineral identified into the solid phase until 15 days. For longer ageing times, nontronite particles rapidly dissolve in favor of the crystallization of aegirine and hematite, until the complete dissolution of nontronite between 31 and 62 days (Fig. 11; Table 1). The possible occurrence of few aegirine crystals into the 1 and 15 days samples remains, however, an open question.

These results on both series reveal that all the synthesized nontronites, whatever their amounts of $^{[4]}\text{Fe(III)}$, appear as metastable phases at 150 °C in this Na-Fe(III)-Si-O-OH system; the stable paragenesis being aegirine and hematite in these experiments. The rate of the reaction nontronite > aegirine + hematite is, however, strongly influenced by the pH of the solution (Fig. 11; Table 1). Similarly, Nagase et al. (1999) synthesized in 1 day at 100 and 200 °C aegirine at pH_f near 13 and nontronite at pH_f near 12. Due to the link between pH_f and the crystal chemistry of nontronites (Baron et al., 2016), nontronites with high levels of $^{[4]}\text{Fe(III)}$ appear as more labile metastable phases than nontronites with low $^{[4]}\text{Fe(III)}$ amounts in the given conditions of the present study. The increase in temperature also favors the formation of aegirine. For similar pH_i near 12, Decarreau et al. (2008, 2004) synthesized nontronites having a $^{[4]}\text{Fe(III)}$ content of 0.75 at temperatures from 75 to 150 °C, and aegirine + ϵ nontronite at 200 °C. Similarly, Kopp and Harris (1967) obtained aegirine at 425 °C and nontronite at 365 °C during the synthesis of grunerite (Fe(II)-amphibole).

This suite of experiments indicates that nontronite is more labile than aegirine in these hydrothermal conditions. However, Eggleton (1975) observed the formation of nontronite at the expense of hedenbergite (Ca-clinopyroxene) in the conditions of Earth’s surface. These

observations show that nanoparticles of nontronite are more stable than pyroxene in weathering conditions. The mineralogical reaction involving nontronite and pyroxene could thus be reversible.

4.2 Thermodynamics: possible explanation of nontronite metastability

In the present study, nontronites form at 150 °C at the early stage of the experiments, although the chemical compositions of solutions are far from the nontronite stability field (Fig. 10). This observation is consistent with the status of nontronite as labile metastable phase, kinetically favored with respect to aegirine, which appears to be the stable silicate, given the conditions of the present study. This reaction pathway looks like it obeys to the Ostwald's step rule (Ostwald, 1897). These results are in agreement with the conclusion of Lippmann (1982, 1979, 1977) and Eberl (1978) indicating that clay minerals can be formed for kinetics reasons far from the thermodynamic equilibrium.

The chemical compositions of solutions during synthesis are located near the tie-line aegirine-hematite or inside the stability field of aegirine (Fig. 10). These data suggest that the chemistry of the solutions is constrained rather by the precipitation of aegirine and that very small amounts of aegirine may form in the early stage of syntheses.

The thermodynamic stability field of nontronite is, however, calculated using “standard” data that do not take into account the effect of particle size. Indeed, it is now well known that the decrease in particle size of a mineral induced modification of its stability field due to change of the surface energy, as observed for alumina (McHale et al., 1997), hydroxyapatite (Tang et al., 2004), TiO₂ (Zhang and Banfield, 1998), and Al- or Fe(III)-[oxi(hydr)]oxide minerals (Trolard and Tardy, 1987; Hochella et al., 2008; Navrotsky et al., 2008). For Fe(III)-[oxi(hydr)]oxides, Navrotsky et al. (2008) concluded: “The competition between surface enthalpy and the energetics of phase transformation leads to the general conclusion that polymorphs metastable as micrometer-sized or larger crystals can often be thermodynamically stabilized at the nanoscale”. Consequently, minerals having high hydration and high surface area can often be formed and thermodynamically stabilized at small particle sizes (Hochella et al., 2008; Navrotsky et al., 2008). Moreover, hydrous minerals can persist and their stability field can significantly expand to higher temperatures if the growth rates of the metastable phase are slower than the phase reaction rate (Hochella et al., 2008; Navrotsky et al., 2008). However, these two studies involved isochemical phase reaction between two polymorphs, which is not the case in our study. Indeed, the reaction observed in our experiments involved for the first time a phyllosilicate (nontronite), an inosilicate (aegirine) and an

oxide (hematite). All assumptions on the isochemical phase reactions are supported by measurements of minerals thermodynamic properties at the nanoscale. However, these data are lacking for nontronite and aegirine + hematite. Nevertheless, we suggest during synthesis experiments, that nontronite probably forms first due to specific thermodynamic properties (surface energy) linked to their very small particles size (nanoparticles) and high hydration properties. At the first stage of synthesis experiments, nanoparticles of nontronite are thermodynamically more competitive to form, but dissolve, when they reach a critical size (100 - 200 nm), in favor of the precipitation of the stable mineral assemblage aegirine + hematite. It is interesting to note that, in experiments at $\text{pH}_i = 12$, the diameter of nontronite particles did not increase markedly (from 50-100 nm up to 200 nm) after six months while the first detected crystals of aegirine in the 183 days sample are already about 500 nm long (Fig. 7h). Nontronite persists only as metastable nanoparticles while stable aegirine crystals enlarge up to more than 3 μm during the same time at $\text{pH}_i = 13.3$ (Fig. 9d).

4.3 Time vs. temperature during nontronite synthesis

In this study, an increase in time of experiments induces an increase in crystallinity (resorption of defects) of synthesized nontronites (see section 3.2.2 and 3.2.3). An equivalent effect of an increase in temperature is observed during similar syntheses of nontronites between 75 and 100 °C (Decarreau et al., 2008), but the increase in temperature up to 150 °C did not induce an increase in crystallinity. These authors concluded that it was not possible to increase the crystallinity of nontronites by increasing the time or the temperature of synthesis. In fact, the metastable nontronite crystals synthesized by Decarreau et al. (2008) had probably reached their critical size before beginning to dissolve in favor of the aegirine crystallization. Klopogge et al. (1999) noted that most of the smectite syntheses do not have sufficient ageing time to ascertain that the synthetic products are the thermodynamically stable phases. These authors also stated that many synthetic products may be metastable, inducing the formation of kinetically favorable phases.

The nontronites synthesized by Decarreau et al. (2008) have been studied for the crystal growth of clay particles, using low-pressure argon adsorption (Decarreau et al. 2014), assuming that time and temperature play equivalent roles. In light of the results of the present study, the role of synthesis time (ageing time) is not necessarily analogous to the one of the temperature during the clay minerals formation in batch experiments.

5 Geological Implications

5.1 Metalliferous sediments, Atlantis II deep, Red Sea

The metalliferous sediments of the Atlantis II deep, Red Sea have been intensively studied since their discovery in 1965 (see an exhaustive review in Laurila et al., 2015). They consist of about 20 m of fine-grained, laminated sediments, composed of oxides, sulfides, silicates, and carbonates, deposited from – 25,000 BP (Anschutz and Blanc, 1995a). These sediments contain detrital and authigenic clays, Fe-nontronites being the most common authigenic ones (Anschutz and Blanc, 1995a; Laurila et al., 2015). Fe-nontronites occur notably in the upper part of sediments (Badaut et al., 1990; Anschutz and Blanc, 1995a). They formed during diagenesis from initial amorphous Si-Fe-O, OH precipitates (Anschutz and Blanc, 1995a; Laurila et al., 2015).

A core (n°684) was collected in 1985 in the western basin of Atlantis II deep during the “Hydrotherm” cruise of the RV Marion Dufresne (Blanc et al., 1986). The porosity of the core remains above 90% in its upper part. Badaut et al. (1992) described, in the core 684, an authigenic Fe-rich nontronite at a depth of 2.6 m ($^{[4]}[\text{Si}_{13.62}\text{Al}_{0.08}\text{Fe(III)}_{0.3}]^{[6]}[\text{Fe(III)}_{1.84}\text{Mg}_{0.13}\text{Al}_{0.03}]\text{O}_{10}(\text{OH})_2[\text{K}_{0.12}\text{Na}_{0.17}(\text{Mg}, \text{Ca})_{0.11}]]$). From oxygen isotopes data, the formation temperature of this nontronite is 70 °C (Decarreau et al., 1990). The chemistry of the pore water of sediments in which the nontronite formed is available ($\text{Si} \approx 100 \mu\text{mol L}^{-1}$, $\text{Na} = 5000 \mu\text{mol L}^{-1}$, $\text{Mg} = 30 \mu\text{mol L}^{-1}$, $\text{K} = 60 \mu\text{mol L}^{-1}$, $\text{Ca} = 130 \mu\text{mol L}^{-1}$, and $\text{pH} = 8.24$) (Blanc et al., 1986; Anschutz and Blanc, 1995b; Anschutz et al., 2000). Activities and speciation of elements in solution were calculated as above for Fig. 10.

The dissolved Na in Atlantis II deep sediments pore water being high, there is a great analogy between authigenic nontronite in the Red Sea and the nontronite syntheses described here. As predicted by Baron et al. (2016), the authigenic nontronite formed at $\text{pH} = 8.24$ would exhibit a low Fe(III) for Si tetrahedral substitution. The chemistry of the pore water was reported on a thermodynamic diagram similar to those used for synthetic nontronites, calculated at 70 °C for a $^{[4]}[\text{Si}_{3.7}\text{Fe(III)}_{0.3}]^{[6]}\text{Fe(III)}_2\text{O}_{10}(\text{OH})_2\text{Na}_{0.3}$ nontronite similar to the nontronite of core 684 (Fig.13). The plot of pore water is located far away from the stability field of nontronite and near the aegirine-hematite (or goethite) equilibrium line, as previously observed for synthetic nontronites (Fig. 10). The Fe-nontronites from the Atlantis II deep are then formed as metastable clay minerals kinetically favored, persisting during more than 10,000 years without any observation of aegirine.

However, the metastable nontronite formed in the Atlantis II deep at a lower temperature than the one used for the synthesis experiments presented here (70 °C instead of 150 °C) and at lower pH (8.24 instead of 12 or 13.3), these two parameters having a strong influence on the kinetic of nontronite > aegirine + hematite reaction (see above). Despite the predominance of Na vs. K, Mg, and Ca in pore water, the exchangeable cations of the nontronite from core 684 are K, Na, and (Mg, Ca) in quite equal amounts. Coupled with the occurrence of octahedral Mg, the nature of these cations may also prevent the dissolution of nontronite in favor of the aegirine crystallization.

5.2 Post-magmatic Fe-clays

Oyawoye & Hirst (1964) observed Fe(III)-rich smectites associated with primary euhedral quartz, feldspars, and biotites in fresh granite. No dissolution features having been observed on the surface of the primary minerals, authors concluded that the Fe(III)-rich smectites had a primary origin. Similarly, Meunier et al. (2008) described nontronite (among other clay minerals) associated with apatites and euhedral pyroxenes in diktytaxitic voids of submarine lava flows. Dissolution features also lacked in these minerals. Because clay minerals were enriched in Rare Earth and incompatible elements, the authors suggested a post-magmatic stage origin of clay minerals at temperatures between 70 and 100 °C. Berger et al. (2014) observed, in other lavas flows, the occurrence of Fe(III)-rich clay minerals having a post-magmatic origin during lava outgassing between 100 and 300 °C. Meunier et al. (2008) and Berger et al. (2014) concluded that anhydrous mafic minerals (pyroxenes) and Fe(III)-clay minerals could be simultaneously formed during these processes, despite the fact that syn-crystallization of hydrated phases with mafic minerals is unusual. In the light of this present study, the syn-formation of pyroxene and Fe(III)-rich clay minerals is possible at a temperature as low as 150 °C. Moreover, the reaction pathway observed suggests that Fe-clays formed first, kinetically favored, and are replaced later by pyroxene.

5.3 Metastability of smectites

Despite the study of the Na-nontronite in the Na-Fe(III)-Si-O-OH at 150 °C, which is not representative of the whole of smectites, some important insights can be obtained from the present experimental study, notably on the role of substitutions on their size and stability. Morse and Casey (1988) and May et al. (1986) proposed that the high chemical heterogeneity of smectites induced their metastability. The present study shows that even in a very simple chemical system, such as

Na-Fe(III)-Si-O-OH, smectite (here nontronite) can be metastable even at a temperature common for smectite formation (i.e., 150 °C). Therefore, the chemical heterogeneity of smectites is not the only parameter responsible for their metastability.

Similarly, Meunier (2006) suggested that the large amounts of crystal defects of clay minerals, notably due to cations substitutions, explained their small particle size. The present study showed that in the case of a smectite with a very simple chemistry (Na-Fe(III)-Si-O-OH), and without any octahedral substitution, the small size of smectite particles is due to their metastability and rather reflects the particle size limit beyond which smectite is dissolved to form the stable mineral assemblage, aegirine + hematite in the context of the present study.

6 Conclusions

For the first time, the metastability of Na-nontronite is evidenced experimentally in the conditions used for this study. Another main point is the mineralogical reaction occurring through an Ostwald's step rule between a metastable phyllosilicate (nontronite) and a stable inosilicate (pyroxene). It is more likely that the crystallization of the Na-nontronite as metastable phase is linked to its nanoscale particle size. Consequently, the use of thermodynamic equilibrium models to predict the formation and evolution of Na-nontronite can be questioned if these models fail to take into account the size dependence of the thermodynamic properties and their effects on the kinetics of reactions (nucleation, growth, phase transition...).

It remains an open question as to whether the results found for Na-nontronite could be generalized to all smectites. Answering this question would require further experimental studies, and most importantly long-time experiments.

Acknowledgments

P. Vieillard and J. Rousseau (IC2MP) are acknowledged for their useful help concerning respectively the calculation of thermodynamic properties of nontronites and the TEM analyses. The European Union (ERDF), "Région Nouvelle Aquitaine", and French « Ministère de l'Enseignement Supérieur et de la Recherche » are also acknowledged for their financial supports.

References

- Aja S. U. and Rosenberg P. E. (1996) The thermodynamic status of compositionally-complex clay minerals; discussion of Clay mineral thermometry; a critical perspective. *Clays Clay Miner.* **44**, 560–568.
- Aja S. U. and Rosenberg P. E. (1992) The thermodynamic status of compositionally-variable clay minerals; a discussion. *Clays Clay Miner.* **40**, 292–299.
- Anschutz P. and Blanc G. (1995a) Chemical mass balances in metalliferous deposits from the Atlantis II Deep, Red Sea. *Geochim. Cosmochim. Acta* **59**, 4205–4218.
- Anschutz P. and Blanc G. (1995b) Geochemical dynamics of the Atlantis II Deep (Red Sea): silica behavior. *Mar. Geol.* **128**, 25–36.
- Anschutz P., Blanc G., Monnin C. and Boulègue J. (2000) Geochemical dynamics of the Atlantis II Deep (Red Sea): II. Composition of metalliferous sediment pore waters. *Geochim. Cosmochim. Acta* **64**, 3995–4006.
- Badaut D., Blanc G. and Decarreau A. (1990) Variation des minéraux argileux ferrifères, en fonction du temps et de l'espace, dans les dépôts métallifères de la fosse Atlantis II en Mer Rouge. *Comptes Rendus Académie Sci. Sér. 2 Mécanique Phys. Chim. Sci. Univers Sci. Terre* **310**, 1069–1075.
- Badaut D., Decarreau A. and Besson G. (1992) Ferripyrophyllite and related Fe^{3+} -rich 2:1 clays in Recent deposits of Atlantis II Deep, Red Sea. *Clay Miner.* **27**, 227–244.
- Baron F., Petit S., Tertre E. and Decarreau A. (2016) Influence of aqueous Si and Fe speciation on tetrahedral Fe(III) substitutions in nontronites: a clay synthesis approach. *Clays Clay Miner.* **64**, 230.
- Berger G., Meunier A. and Beaufort D. (2014) Clay mineral formation on Mars: Chemical constraints and possible contribution of basalt out-gassing. *Planet. Space Sci.* **95**, 25–32.
- Blanc G., Boulègue J., Badaut D. and Stouff P. (1986) Premiers résultats de la campagne océanographique Hydrocherm (mai 1985) du Marion-Dufresne sur la fosse Aûancis II (Mer Rouge). *Comptes Rendus Académie Sci. - Ser. IIA - Earth Planet. Sci.* **302**, 175–180.
- Blanc P., Vieillard P., Gailhanou H., Gaboreau S., Gaucher É., Fialips C. I., Madé B. and Giffaut E. (2015) A generalized model for predicting the thermodynamic properties of clay minerals. *Am. J. Sci.* **315**, 734–780.
- Brigatti M. F. (1983) Relationships between composition and structure in Fe-rich smectites. *Clay Miner.* **18**, 177–186.

553 Brindley G. W. and Brown G. (1980) *Crystal structures of clay minerals and their X-ray*
554 *identification*. Monograph no. 5., Mineralogical Society, London.

555 Carter J., Loizeau D., Mangold N., Poulet F. and Bibring J.-P. (2015) Widespread surface
556 weathering on early Mars: A case for a warmer and wetter climate. *Icarus* **248**, 373–382.

557 Carter J., Poulet F., Bibring J.-P., Mangold N. and Murchie S. (2013) Hydrous minerals on Mars
558 as seen by the CRISM and OMEGA imaging spectrometers: Updated global view. *J.*
559 *Geophys. Res. Planets* **118**, 831–858.

560 Clark J. R., Appleman D. E. and Papike J. J. (1969) Crystal-chemical characterization of
561 clinopyroxenes based on eight new structure refinements. *Mineral. Soc. Am. - Spec. Pap.*
562 **2**, 31–50.

563 Decarreau A. (1985) Partitioning of divalent transition elements between octahedral sheets of
564 trioctahedral smectites and water. *Geochim. Cosmochim. Acta* **49**, 1537–1544.

565 Decarreau A., Badaut D. and Blanc G. (1990) Origin and temperature formation of Fe-rich clays
566 from Atlantis II deep deposits (Red Sea). An oxygen isotopic geochemistry approach.
567 *Chem. Geol.* **84**, 363–364.

568 Decarreau A., Petit S., Andrieux P., Villieras F., Pelletier M. and Razafitianamaharavo A. (2014)
569 Study of lox-pressure argon adsorption on synthetic nontronite: Implications for smectite
570 crystal growth. *Clays Clay Miner.* **62**, 102–111.

571 Decarreau A., Petit S., Martin F., Farges F., Vieillard P. and Joussein E. (2008) Hydrothermal
572 synthesis, between 75 and 150 °C, of high-charge, ferric nontronites. *Clays Clay Miner.*
573 **56**, 322–337.

574 Decarreau A., Petit S., Vieillard P. and Dabert N. (2004) Hydrothermal synthesis of aegirine at
575 200 °C. *Eur. J. Mineral.* **16**, 85–90.

576 Eberl D. (1978) Reaction series for dioctahedral smectites. *Clays Clay Miner.* **26**, 327–340.

577 Eggleton R. A. (1977) Nontronite; chemistry and X-ray diffraction. *Clay Miner.* **12**, 181–194.

578 Eggleton R. A. (1975) Nontronite topotaxial after hedenbergite. *Am. Mineral.* **60**, 1063–1068.

579 Essene E. J. and Peacor D. R. (1995) Clay mineral thermometry; a critical perspective. *Clays*
580 *Clay Miner.* **43**, 540–553.

581 Essene E. J. and Peacor D. R. (1997) Illite and smectite; metastable, stable or unstable? Further
582 discussion and a correction; reply. *Clays Clay Miner.* **45**, 116–122.

583 Gates W. P. (2008) Cation mass-valence sum (CM-VS) approach to assigning OH-bending bands
 584 in dioctahedral smectites. *Clays Clay Miner.* **56**, 10–22.

585 Gates W. P. (2005) The Application of Vibrational Spectroscopy to Clay Minerals and Layered
 586 Double Hydroxides. In *Infrared spectroscopy and the chemistry of dioctahedral smectites*
 587 (ed. J. Theo Kloprogge). The Clay Minerals Society, Aurora, CO. pp. 125–168.

588 Goodman B. A., Russell J. D., Fraser A. R. and Woodhams F. W. D. (1976) A Mössbauer and
 589 I.R. spectroscopic study of the structure of nontronite. *Clays Clay Miner.* **24**, 53–59.

590 Gunnarsson I. and Arnórsson S. (2000) Amorphous silica solubility and the thermodynamic
 591 properties of H_4SiO_4 in the range of 0 to 350 °C at P_{sat} . *Geochim. Cosmochim. Acta* **64**,
 592 2295–2307.

593 Hemingway B. S. (1990) Thermodynamic properties for bunsenite, NiO, magnetite, Fe_3O_4 , and
 594 hematite, Fe_2O_3 , with comments on selected oxygen buffer reactions. *Am. Mineral.* **75**,
 595 781–790.

596 Heuser M., Andrieux P., Petit S. and Stanjek H. (2013) Iron-bearing smectites: a revised
 597 relationship between structural Fe, b cell edge lengths and refractive indices. *Clay Miner.*
 598 **48**, 97–103.

599 Hochella M. F., Lower S. K., Maurice P. A., Penn R. L., Sahai N., Sparks D. L. and Twining B.
 600 S. (2008) Nanominerals, Mineral Nanoparticles, and Earth Systems. *Science* **319**, 1631–
 601 1635.

602 Kittrick J. A. (1971a) Montmorillonite Equilibria and the Weathering Environment. *Soil Sci. Soc.*
 603 *Am. J.* **35**, 815–820.

604 Kittrick J. A. (1971b) Stability of Montmorillonites: I. Belle Fourche and Clay Spur
 605 Montmorillonites. *Soil Sci. Soc. Am. J.* **35**, 140–145.

606 Kittrick J. A. (1971c) Stability of Montmorillonites: II. Aberdeen Montmorillonite. *Soil Sci. Soc.*
 607 *Am. J.* **35**, 820–823.

608 Kittrick J. A. and Peryea F. J. (1988) Experimental Validation of the Monophase Structure Model
 609 for Montmorillonite Solubility. *Soil Sci. Soc. Am. J.* **52**, 1199–1201.

610 Kittrick J. A. and Peryea F. J. (1989) The Monophase Model for Magnesium-Saturated
 611 Montmorillonite. *Soil Sci. Soc. Am. J.* **53**, 292–295.

612 Kloprogge J. T., Komarneni S. and Amonette J. E. (1999) Synthesis of smectite clay minerals; a
 613 critical review. *Clays Clay Miner.* **47**, 529–554.

614 Kopp O. C. and Harris L. A. (1967) Synthesis of Grunerite and Other Phases in the System SiO₂-
615 NaOH-Fe-HaO. *Am. Mineral.* **52**, 1681–1688.

616 Köster H. M., Ehrlicher U., Gilg H. A., Jordan R., Murad E. and Onnich K. (1999) Mineralogical
617 and chemical characteristics of five nontronites and Fe-rich smectites. *Clay Miner.* **34**,
618 579–599.

619 Laurila T. E., Hannington M. D., Leybourne M., Petersen S., Devey C. W. and Garbe-Schönberg
620 D. (2015) New insights into the mineralogy of the Atlantis II Deep metalliferous
621 sediments, Red Sea. *Geochim. Geophys. Geosystems* **16**, 4449–4478.

622 Lippmann F. (1979) Stability diagrams involving clay minerals. In *Eighth Conference on Clay*
623 *Mineralogy and Petrology in Teplice* Pragues. pp. 153–171.

624 Lippmann F. (1977) The solubility products of complex minerals, mixed crystals, and three-layer
625 clay minerals. *Neues Jahrb. Für Mineral. - Abh.* **130**, 243–263.

626 Lippmann F. (1982) The thermodynamic status of clay minerals. In *Proceedings of the 7th*
627 *International Clay Conference, 1981* Developments in sedimentology. Elsevier,
628 Amsterdam. pp. 475–485.

629 Madejová J., Gates W. P. and Petit S. (2017) IR Spectra of Clay Minerals. In *Developments in*
630 *Clay Science* (eds. W. P. Gates, J. T. Kloprogge, J. Madejová, and F. Bergaya). Infrared
631 and Raman Spectroscopies of Clay Minerals. Elsevier. pp. 107–149.

632 May H. M., Klennburgh D. G., Helmke P. A. and Jackson M. L. (1986) Aqueous dissolution,
633 solubilities and thermodynamic stabilities of common aluminosilicate clay minerals:
634 Kaolinite and smectites. *Geochim. Cosmochim. Acta* **50**, 1667–1677.

635 McHale J. M., Auroux A., Perrotta A. J. and Navrotsky A. (1997) Surface Energies and
636 Thermodynamic Phase Stability in Nanocrystalline Aluminas. *Science* **277**, 788–791.

637 Meunier A. (2006) Why are clay minerals small? *Clay Miner.* **41**, 551–566.

638 Meunier A., Mas A., Beaufort D., Patrier P. and Dudoignon P. (2008) Clay minerals in basalt-
639 hawaiiite rocks from Mururoa Atoll (French Polynesia). II. Petrography and
640 Geochemistry. *Clays Clay Miner.* **56**, 730–750.

641 Meunier A., Petit S., Ehlmann B. L., Dudoignon P., Westall F., Mas A., El Albani A. and Ferrage
642 E. (2012) Magmatic precipitation as a possible origin of Noachian clays on Mars. *Nat.*
643 *Geosci.* **5**, 739–743.

- Michalski J. R., Cuadros J., Bishop J. L., Darby Dyar M., Dekov V. and Fiore S. (2015) Constraints on the crystal-chemistry of Fe/Mg-rich smectitic clays on Mars and links to global alteration trends. *Earth Planet. Sci. Lett.* **427**, 215–225.
- Morse J. W. and Casey W. H. (1988) Ostwald processes and mineral paragenesis in sediments. *Am. J. Sci.* **288**, 537–560.
- Mustard J. F., Murchie S. L., Pelkey S. M., Ehlmann B. L., Milliken R. E., Grant J. A., Bibring J.-P., Poulet F., Bishop J., Dobrea E. N., Roach L., Seelos F., Arvidson R. E., Wiseman S., Green R., Hash C., Humm D., Malaret E., McGovern J. A., Seelos K., Clancy T., Clark R., Marais D. D., Izenberg N., Knudson A., Langevin Y., Martin T., McGuire P., Morris R., Robinson M., Roush T., Smith M., Swayze G., Taylor H., Titus T. and Wolff M. (2008) Hydrated silicate minerals on Mars observed by the Mars Reconnaissance Orbiter CRISM instrument. *Nature* **454**, 305–309.
- Nagase T., Iwasaki T., Ebina T., Hayashi H., Onodera Y. and Dutta N. C. (1999) Hydrothermal synthesis of Fe-montmorillonite in Si-Fe-Mg system. *Chem. Lett.* **28**, 303–304.
- Navrotsky A., Mazeina L. and Majzlan J. (2008) Size-Driven Structural and Thermodynamic Complexity in Iron Oxides. *Science* **319**, 1635–1638.
- Neumann, A., Petit, S., & Hofstetter, T.B. (2011) Evaluation of redox-active iron sites in smectites using middle and near infrared spectroscopy. *Geochimica et Cosmochimica Acta*, **75**, 2336–2355.
- Nolan J. (1969) Physical properties of synthetic and natural pyroxenes in the system diopside-hedenbergite-acmite. *Mineral. Mag.* **37**, 216–229.
- Nývlt J. (1995) The Ostwald Rule of Stages. *Cryst. Res. Technol.* **30**, 443–449.
- Ostwald W. (1897) Studien über die Bildung und Umwandlung fester Körper. 1. Abhandlung: Übersättigung und Überkaltung. *Z. Für Phys. Chem.* **22**, 289–330.
- Oyawoye M. O. and Hirst D. M. (1964) Occurrence of a montmorillonite mineral in the Nigerian younger granites at Ropp, Plateau Province, Northern Nigeria. *Clay Miner.* **5**, 427–433.
- Parkhurst D. L. and Appelo C. A. J. (2013) Description of input and examples for PHREEQC version 3 — A computer program for speciation, batch-reaction, one-dimensional transport, and inverse geochemical calculations. *US Geol. Surv. Tech. Methods*.
- Petit S., Baron F. and Decarreau A. (2017) Synthesis of nontronite and other Fe-rich smectites: a critical review. *Clay Miner.* **52**, 469–483.

675 Petit S., Decarreau A., Gates W., Andrieux P. and Grauby O. (2015) Hydrothermal synthesis of
 676 dioctahedral smectites: The Al–Fe³⁺ chemical series. Part II: Crystal-chemistry. *Appl.*
 677 *Clay Sci.* **104**, 96–105.

678 Poulet F., Bibring J.-P., Mustard J. F., Gendrin A., Mangold N., Langevin Y., Arvidson R. E.,
 679 Gondet B. and Gomez C. (2005) Phyllosilicates on Mars and implications for early
 680 martian climate. *Nature* **438**, 623–627.

681 Redhammer G. J., Amthauer G., Lottermoser W. and Treutmann W. (2000) Synthesis and
 682 structural properties of clinopyroxenes of the hedenbergite CaFe²⁺Si₂O₆ - aegirine
 683 NaFe³⁺Si₂O₆ solid-solution series. *Eur. J. Mineral.* **12**, 105–120.

684 Robie R. A. and Hemingway B. S. (1995) *Thermodynamic properties of minerals and related*
 685 *substances at 298.15 K and 1 bar (10⁵ pascals) pressure and at higher temperatures.*
 686 USGS Bulletin 2131, 461 p.

687 Strickland J. D. H. and Parsons T. R. (1972) *A practical handbook of seawater analysis*, Fisheries
 688 Research Board of Canada, Ottawa.

689 Stucki, J.W., Goodman, B.A., & Schwertmann, U. (Eds.) (1988) *Iron in Soils and Clay Minerals*,
 690 Dordrecht, Holland.

691 Stucki, J.W. (2013) Properties and behaviour of iron in clay minerals. Pp. 559–612 in: *Handbook*
 692 *of Clay Science* (Bergaya, F. and Lagaly, G. editors). Elsevier, Amsterdam.

693 Tang R., Wang L. and Nancollas G. H. (2004) Size-effects in the dissolution of hydroxyapatite:
 694 an understanding of biological demineralization. *J. Mater. Chem.* **14**, 2341–2346.

695 Thompson J. B. (1955) The thermodynamic basis for the mineral facies concept. *Am. J. Sci.* **53**,
 696 65–103.

697 Trolard F. and Tardy Y. (1987) The stabilities of gibbsite, boehmite, aluminous goethites and
 698 aluminous hematites in bauxites, ferricretes and laterites as a function of water activity,
 699 temperature and particle size. *Geochim. Cosmochim. Acta* **51**, 945–957.

700 Van Santen R. A. (1984) The Ostwald step rule. *J. Phys. Chem.* **88**, 5768–5769.

701 Wilson M. J. (2013) *Sheet Silicates: Clay Minerals*. The Geological Society. eds. Deer, Howie,
 702 and J. Zussman, The Geological Society, London.

703 Zhang H. and Banfield J. F. (1998) Thermodynamic analysis of phase stability of nanocrystalline
 704 titania. *J. Mater. Chem.* **8**, 2073–2076.

Zhang M., Redhammer J. G., Salje H. E. K. and Mookherjee M. (2002) $\text{LiFeSi}_2\text{O}_6$ and $\text{NaFeSi}_2\text{O}_6$ at low temperatures: an infrared spectroscopic study. *Phys. Chem. Miner.* **29**, 609–616.

Figure captions:

Figure 1: Structure of the Na-nontronite.

Figure 2: XRD powder patterns (a) of the series of samples synthesized at $\text{pH}_i = 12$. (b): zoom of the (06,33) reflection.

Figure 31: XRD powder patterns (a) of the series of samples synthesized at $\text{pH}_i = 13.3$. (b): zoom of the (06,33) reflection.

Figure 4: MIR spectra of the gel precursor and of a synthesized nontronite (NT10).

Figure 5: TEM images of the starting gel.

Figure 6: MIR spectra of the series of samples synthesized at $\text{pH}_i = 12$.

Figure 7: TEM images of the series of samples synthesized at $\text{pH}_i = 12$ for different synthesis times: NT42 - 1 day (a, b); NT0 - 6 days (c, d); NT28 - 31 days (e, f); and NT33 - 183 days (g, h).

Figure 8: MIR spectra of the series of samples synthesized at $\text{pH}_i = 13.3$.

Figure 9: TEM images of the series of samples synthesized at $\text{pH}_i = 13.3$ for different synthesis times: NT41 - 1 day (a, b, c); NT32 - 31 days (d, e, f); and NT35 - 183 days (g, h). (a) A = nontronite particles with around 50 nm in diameter; B = nontronite particles with hundreds nm in diameter.

Figure 10: Thermodynamic stability diagrams at 150 °C of aegirine ($\text{Si}_2\text{Fe(III)NaO}_6$), hematite (Fe_2O_3), ferripyrophyllite ($\text{Si}_4^{[6]}\text{Fe(III)}_2\text{O}_{10}(\text{OH})_2$), and nontronite $[\text{Si}_{4-x}^{[4]}\text{Fe(III)}_x]^{[6]}\text{Fe(III)}_2\text{O}_{10}(\text{OH})_2\text{Na}_x$. (a) nontronite with $x = 0.5$ (black lines) and $x = 0.75$ (grey lines). (b) nontronite with $x = 1.15$ (black lines) and $x = 1.35$ (grey lines). Black dots correspond to chemical solutions at the end of experiments. The estimated errors are given by the diameter of black dots. Solubility line of amorphous silica was plotted according to Gunnarsson and Arnórsson (2000).

Figure 11: Relative amounts of solid phases (arbitrary units) successively observed at different times of synthesis, at 150 °C, in the Si-Fe(III)-Na system.

Figure 12: Amounts of tetrahedral iron ($^{[4]}\text{Fe(III)}$) in synthetic nontronites vs. the end of synthesis pH (pH_f).

744
745 Figure 13: Thermodynamic stability diagrams at 70 °C of aegirine, hematite, ferripyrophyllite, and
746 nontronite $[\text{Si}_{3.7}^{[4]}\text{Fe(III)}_{0.3}]^{[6]}\text{Fe(III)}_2\text{O}_{10}(\text{OH})_2\text{Na}_{0.3}$. Empty circle corresponds to the chemistry
747 of the pore water core 684 in sediments of Atlantis II deep, Red Sea (Data from Blanc et al. (1986);
748 Anschulz et al., (1995, 2000)).